

Low/Hard State Spectra of GRO J1655-40 Observed with Suzaku

Hiromitsu TAKAHASHI¹, Yasushi FUKAZAWA¹, Tsunefumi MIZUNO¹, Ayumi HIRASAWA¹
Shunji KITAMOTO², Keisuke SUDOH², Takayuki OGITA²

Aya KUBOTA³, Kazuo MAKISHIMA^{4,5}, Takeshi ITOH⁵,

Arvind N. PARMAR⁶, Ken EBISAWA⁷, Sachindra NAIK⁷, Tadayasu DOTANI⁷, Motohide KOKUBUN⁷

Kousuke OHNUKI⁷, Tadayuki TAKAHASHI⁷, Tahir YAQOOB⁸, Lorella ANGELINI⁹

Yoshihiro UEDA¹⁰, Kazutaka YAMAOKA¹¹, Taro KOTANI¹², Nobuyuki KAWAI¹²

Masaaki NAMIKI¹³, Takayoshi KOHMURA¹⁴, Hitoshi NEGORO¹⁵

¹ *Department of Physical Science, School of Science, Hiroshima University
1-3-1 Kagamiyama, Higashi-Hiroshima, Hiroshima 739-8526, Japan*

² *Department of Physics, Rikkyo University*

3-34-1, Nishi-Ikebukuro, Toshima-ku, Tokyo 171-8501, Japan

³ *Department of Electronic Information Systems, Shibaura Institute of Technology
307 Fukasaku, Minuma-ku, Saitama-shi, Saitama 337-8570, Japan*

⁴ *Cosmic Radiation Laboratory, Institute of Physical and Chemical Research (RIKEN)
2-1 Hirosawa, Wako-shi, Saitama, 351-0198, Japan*

⁵ *Department of Physics, University of Tokyo*

7-3-1, Hongo, Bunkyo-ku, Tokyo, 113-0033, Japan

⁶ *Astrophysics Mission Division, Research and Scientific Support Department of ESA, ESTEC
Postbus 299, NL-2200 AG Noordwijk, The Netherlands*

⁷ *Institute of Space and Astronautical Science, JAXA*

3-1-1, Yoshinodai, Sagamihara, Kanagawa, 229-8510, Japan

⁸ *Department of Physics and Astronomy, John Hopkins University
3400 N, Charles St., Baltimore, MD 21218, USA*

⁹ *Explosion of the Universe Division, NASA Goddard Space Flight Center
Greenbelt, MD 20771, USA*

¹⁰ *Department of Astronomy, Kyoto University*

Kitashirakawa-Oiwake-cho, Sakyo-ku, Kyoto, 606-8502, Japan

¹¹ *Department of Physics & Mathematics, Aoyama Gakuin University
5-10-1 Sagamihara, Kanagawa, 229-8558, Japan*

¹² *Department of Physics, Tokyo Institute of Technology*

2-12-1, O-okayama, Meguro-ku, Tokyo, 152-8551, Japan

¹³ *Department of Earth and Space Science, Graduate School of Science, Osaka University
1-1, Machikaneyama, Toyonaka, Osaka, 560-0043, Japan*

¹⁴ *Physics Department, Kogakuin University*

2665-1, Nakano-cho, Hachioji, Tokyo, 192-0015, Japan

¹⁵ *Department of Physics, College of Science and Technology, Nihon University
1-8, Kanda-Surugadai, Chiyoda-ku, Tokyo, 101-8308, Japan*

Abstract

The Galactic black-hole binary GRO J1655–40, a source harboring superluminal jets, was observed with Suzaku on 2005 September 22–23, for a total time span of ~ 1 day, and a net exposure of 35 ks with the X-ray Imaging Spectrometer (XIS) and 20 ks with the Hard X-ray Detector (HXD). The source was detected over a broad and continuous energy range of 0.7–300 keV, with an intensity of ~ 50 mCrab at 20 keV. At a distance of 3.2 kpc, the 0.7–300 keV luminosity is $\sim 5.1 \times 10^{36}$ erg s $^{-1}$ (~ 0.7 % of the Eddington luminosity for a $6 M_{\odot}$ black hole). The source was in a typical low/hard state, exhibiting a power-law shaped continuum with a photon index of ~ 1.6 . During the observation, the source intensity gradually decreased by 25% at energies above ~ 3 keV, and by 35% below 2 keV. This, together with the soft X-ray spectra taken with the XIS, suggests the presence of an independent soft component that can be represented by emission from a cool (~ 0.2 keV) disk. The hard X-ray spectra obtained with the HXD reveal a high-energy spectral cutoff, with an e-folding energy of ~ 200 keV. Since the spectral photon index above 10 keV is harder by ~ 0.4 than that observed in the softer energy band, and the e-folding energy is higher than those of typical reflection humps, the entire 0.7–300 keV spectrum cannot be reproduced by a single thermal Comptonization model, even considering reflection effects. Instead, the spectrum (except the soft excess) can be successfully explained by invoking two thermal-Comptonization components with different y -parameters. In contrast to the high/soft state spectra of this object in which narrow iron absorption lines are detected with equivalent widths of 60–100 eV, the present XIS spectra bear no such features beyond an upper-limit equivalent width of 25 eV.

Key words: accretion disks — black hole physics — stars: individual (GRO J1655-40)— X-ray: binaries

1. Introduction

X-ray spectra of black-hole binaries (BHBs) depend on the luminosity in complex ways, particularly when they are luminous (e.g., Fender et al. 2004; Kubota & Makishima 2004). However, as long as the luminosity is well below the Eddington limit, L_E , BHBs exhibit only two major spectral states; the high/soft state and the low/hard state, which manifest themselves when the luminosity is higher and lower than a few percent of L_E , respectively (Tanaka & Shibazaki 1996; McClintock & Remillard 2003). In the high/soft state, a BHB spectrum consists of optically-thick thermal emission from a standard accretion disk (e.g., Makishima et al. 1986), and a power-law shaped hard tail extending up to MeV energies with a photon index of $\Gamma \sim 2.3$.

In the low/hard state, a BHB emits a harder spectrum that can be approximated by a $\Gamma \sim 1.7$ power law, accompanied by subsidiary features such as iron-K related structures (e.g., Ebisawa et al. 1996), a low energy excess (e.g., Balucinska-Church et al. 1995), and a hard X-ray hump attributable to reflection by cool matter (e.g., Frontera et al. 2001; Lightman & White 1988). In addition, the spectrum often exhibits a cutoff at energies above 50–150 keV, as observed from several BHBs and a fair number of Seyfert galaxies (e.g., Quadrelli et al. 2003; Risaliti 2002). As a result, a thermal-Comptonization scenario (e.g., Sunyaev & Titarchuk 1980; Poutanen & Svensson 1996; Zdziarski et al. 1996) and its variants have been developed as a standard interpretation. According to this scenario, the low/hard state emission from an accreting black hole is formed when some seed photons are Compton up-scattered by a hot electron distribution, with the electron temperature determining the high-energy spectral cutoff.

In spite of its general success, details of the thermal Comptonization scenario are far from established. It is yet to be clarified whether the supposed hot electron cloud should be identified with an optically-thin portion of the accretion disk, or a sort of corona above an optically-thick cool disk. The radial and vertical extents of the hot cloud are not well constrained. Nor is it clear yet whether the soft seed photons come from an optically-thick and cool portion of the disk, or from the hot cloud itself as thermal cyclotron emission. In order to better quantify this promising scenario for the low/hard state, careful modeling of the spectra over a broad energy band is of particular importance. In fact, Frontera et al. (2001) found that broad-band spectra of Cyg X-1, obtained with BeppoSAX, can be successfully reproduced by invoking *two* Compton y -parameters, of 0.15 and 0.89. We may then utilize the extremely broad energy band of Suzaku (Mitsuda et al. 2007), to extend such studies to a larger number of BHBs. Here, we describe Suzaku results on the low/hard state of GRO J1655–40, which is a secure BHB having a much higher inclination angle than Cyg X-1 ($20^\circ \sim 65^\circ$; Gies & Bolton 1986; Ninkov et al. 1987).

GRO J1655–40 is a transient X-ray source discovered with the BATSE onboard the

Compton Gamma Ray Observatory (Zhang et al. 1994). Subsequent optical observations revealed a 2.6 d binary period (Bailyn et al. 1995), and successfully determined the mass of the compact object and mass-donating star as $5.5 - 7.9 M_{\odot}$ and $1.7 - 3.3 M_{\odot}$, respectively (Shahbaz et al. 1999). The system is thus considered to be a BHB. Together with GRS 1915+105 (Mirabel & Rodriguez 1994), this object is classified as an interesting subgroup of BHB possessing superluminal radio jets (Hjellming & Rupen 1995). The system inclination, i , of GRO J1655–40 is estimated to be 85° from jet kinematics, or $\sim 70^{\circ}$ from optical light curves (van der Hooft et al. 1998). Although the distance is estimated to be 3.2 ± 0.2 kpc from the radio jet kinematics (Hjellming & Rupen 1995), a shorter distance of $\lesssim 1.7$ kpc has been proposed by Foellmi et al. (2006) based on the spectral type of the secondary star. In addition, GRO J1655–40 allowed the first detection of narrow X-ray absorption lines from ionized iron (Ueda et al. 1998; Yamaoka et al. 2001). Together with those in other high-inclination sources (Kotani et al. 2000; Ueda et al. 2001) and in dipping binary sources (Diaz Trigo et al. 2006), the detection of these absorption lines indicates the existence of highly ionized plasmas above the accretion disks.

On 2005 February 17, an X-ray brightening of GRO J1655-40 was detected by the RXTE All Sky Monitor (ASM) (Markwardt et al. 2005); since then it remained active for more than half a year. X-ray observations were carried out with XMM-Newton (Diaz Trigo et al. 2007; Sala et al. 2007), INTEGRAL (Diaz Trigo et al. 2007; Shaposhnikov et al. 2007), Swift (Brocksopp et al. 2006), Chandra (Miller et al. 2006b), and RXTE (Shaposhnikov et al. 2007), as the source evolved from the low/hard state into the high/soft state, and then back again. Based on high energy spectra obtained in the low/hard state early in the outburst, Shaposhnikov et al. (2007) reported the detection of a high-energy cutoff around 180 keV. In contrast, broad-band spectra taken during the high/soft state reveal a hard tail component extending up to ~ 150 keV (Brocksopp et al. 2006; Diaz Trigo et al. 2007), reconfirming a previous OSSE detection (Kroeger et al. 1996; Zhang et al. 1997). The absorption lines from highly ionized ions were also reconfirmed with a blue shift equivalent to $300\text{-}6000$ km s $^{-1}$ (Miller et al. 2006b; Diaz Trigo et al. 2007; Sala et al. 2007).

The present paper describes Suzaku observations of GRO J1655 – 40 made in the decay phase during the 2005 September campaign, while the object was in the low/hard state. We successfully detected the object over a broad, unprecedented, energy range of 0.7–300 keV. Although the obtained broad-band spectra can be approximated by a power-law of photon index ~ 1.6 , the high-quality Suzaku data clearly reconfirm the spectral cutoff at energies above ~ 100 keV as well as a weak soft X-ray excess. Furthermore, the data require two Comptonized components, having a common electron temperature but different optical depths. Absorption features around 6 keV were not detected significantly.

2. Observation

Using Suzaku (Mitsuda et al. 2007), we observed GRO J1655–40 from 2005 September 22, 07:16 UT, through 07:07 UT of the next day. The data were acquired with the X-ray Imaging Spectrometer (XIS: Koyama et al. 2007) and the Hard X-ray Detector (HXD: Takahashi et al. 2007; Kokubun et al. 2007). As shown in figure 1, the source was at that time in the decay phase of the 2005 outburst, exhibiting a typical 1.5–12 keV intensity of a few tens mCrab.

Installed at the focal plane of the four X-ray telescopes (XRT: Serlemitsos et al. 2007), the XIS consists of one back-illuminated CCD (BI-CCD) camera and three front-illuminated CCD (FI-CCD) cameras, observing in the energy range from 0.2 keV to 12 keV. During the present GRO J1655–40 observation, the XIS was operated in the normal 3×3 and 2×2 modes. Since the source is relatively bright, we employed “1/8 window” option in which, out of the 1024 rows, 128 rows around the source image are read out. This shortens the frame exposure time to 1 s, and reduces the number of XIS events suffering from pile-up. Furthermore, one of the FI-CCDs (XIS0) was not used in order to double the telemetry capacity of the BI-CCD (XIS1).

The HXD was operated in the normal mode, acquiring 10–70 keV data with the Si PIN photo diodes (hereafter PIN) and 40–600 keV data with the GSO scintillators (hereafter GSO). Combining PIN and GSO with the XIS, Suzaku can cover a broad energy band spanning three orders of magnitude.

The average 0.7–300 keV flux of GRO J1655–40 was measured to be 4.0×10^{-9} erg $\text{s}^{-1} \text{cm}^{-2}$. The luminosity in the same band was estimated to be 5.1×10^{36} erg s^{-1} , which corresponds to $\sim 0.7\%$ of L_E for a $6 M_\odot$ black hole, assuming a distance of 3.2 kpc (Hjellming & Rupen 1995).

3. Data Analysis and Results

3.1. Data Selection and Background Subtraction

For the XIS data analysis, we accumulated cleaned events over good time intervals that were selected by removing spacecraft passages through the South Atlantic Anomaly (SAA) and periods of low earth elevation ($< 20^\circ$ for the day-time earth and $< 5^\circ$ for the night earth). The details are described in Fujimoto et al. (2007). The source and background events were accumulated inside and outside the central circular region of radius $4'.3$ for each CCD image, respectively. Since XIS2 and XIS3 have almost the same properties, we hereafter present results obtained from their co-added spectra. The total exposure time achieved was 35 ks per sensor.

Although the intensity of GRO J1655–40 was ~ 50 mCrab and we used the “1/8 window” option, we still need to be careful about photon pile-up in the XIS data. In order to quantify this effect, we tentatively extracted another spectrum from a $1'.0 - 4'.3$ annular region, where the count rate for each pixel is several times lower than that within the central $1'.0$, and the

pile-up effect is considered to be negligible in the annulus. Comparing this spectrum with the original one from the entire $4'.3$ radius, we found that the original spectrum has $\sim 3\%$ and 5% higher count rates than the annular one in the 7–8 keV and 9–10 keV energy bands, respectively, after equalizing their normalizations in the 1–2 keV band. This result suggests that the region inside $1'$ slightly suffers from photon pile-up. Therefore, considering the statistical error ($\sim 3\%$) of the spectra after binning, we limited the XIS energy range to < 8 keV.

Since the HXD does not have offset detectors (Takahashi et al. 2007), subtraction of non X-ray background is an essential part of the data analysis. Generally, the background spectrum to be subtracted is synthesized, employing certain models that are based on the HXD data accumulated during periods of Earth occultation (Kokubun et al. 2007). The models are being developed by the HXD team, and the results are being made publicly available ¹; some early Suzaku publications (e.g., Reeves et al. 2007; Miniutti et al. 2007) have actually used the modeled PIN backgrounds. However, GRO J1655–40 was observed only 2 months after the launch, when long-lived activation components in the GSO background spectra were still increasing at a significant rate. Therefore, the model background is thought to be less reliable in this particular case, compared to other HXD observations conducted on later occasions. We have hence chosen another method, namely to derive the background spectrum directly from some blank-sky observations conducted on an occasion close in time to the present observation of GRO J1655–40. Below, our primary method is to employ this blank-sky subtraction, but we will compare our results to the “standard” modeled background as a cross confirmation.

To carry out the blank-sky subtraction, we employed data from an observation of the planetary nebula BD+30°3639, because it was conducted on the day just before the GRO J1655–40 observation (2006 September 21), and no hard X-ray source is catalogued in this sky region. The on-source (i.e., GRO J1655–40) and blank-sky (i.e., BD+30°3639) data were both accumulated after removing time periods immediately before (3 minutes) and after (7 minutes) each passage through the SAA, and those periods when Suzaku was in regions of low geomagnetic cutoff rigidity (< 8 GV). To exclude the periods of Earth occultation, we further screened the on-source data by the condition that the target elevation above the Earth’s horizon should be $> 5^\circ$. Then, the background events of PIN and GSO were accumulated over the same orbital phases of Suzaku as the on-source data integration. The obtained on-source exposure was corrected for dead time, using so-called pseudo events implemented in the HXD (Takahashi et al. 2007); this method has been verified in orbit using other independent dead-time indicators (Kokubun et al. 2007). As a result, a live time of 20 ks was attained.

Figure 2 compares the on-source and blank-sky HXD spectra, both obtained in this way. The background-subtracted spectra are also presented. The source is so bright that the signal from GRO J1655–40 is more than half of the PIN background even at its upper-bound energy of 70 keV. Therefore, systematic errors of the PIN background are considered to be negligible

¹ <http://www.astro.isas.jaxa.jp/suzaku/analysis/hxd/hxdnxb/>

over the entire PIN energy range (10–70 keV). In the GSO range, the source signal is 25% and 10% of the background at 40–100 keV and 100–300 keV, respectively. As described in the Appendix, the GSO background estimation using blank-sky observations is thought to be accurate to about 2%. As a result, we can claim a source detection with the GSO over an energy range of 40–300 keV. Since the GSO background subtraction becomes more susceptible to systematic errors as the integration time becomes shorter, we hereafter report results from analysis of the GSO data integrated over the entire 20 ks exposure only.

In addition to the above analysis using the blank-sky observation, we tried currently available background models to synthesize the PIN and GSO backgrounds. These models provide a set of time-tagged *fake* events (separately for PIN and GSO), in the same form as the actual on-source data acquired. We processed these background events in exactly the same manner as the on-source data, using in particular the same “good time intervals”. The derived model backgrounds are also presented in figure 2. Thus, the two sets of backgrounds from the two methods (the blank-sky data and the synthetic model) agree well with each other; the GSO backgrounds agree within $\lesssim 2\%$, while the PIN spectra agree within $\lesssim 3\%$ below ~ 50 keV, although there is a slight deviation at higher energies.

3.2. Energy Spectra

Figure 3 shows broad-band energy spectra of GRO J1655–40 from 0.7 keV to 300 keV, obtained with the XIS and HXD, by averaging all the data. In order to assess the overall shapes of these spectra without relying on the detector responses and in a way that is rather free from possible calibration uncertainties, we first converted them into so-called “Crab ratios”, whereby the source spectrum is divided by a Crab spectrum that was accumulated in the same way. As shown in figure 4, the calculated Crab ratio indicates that the object had an intensity of ~ 50 mCrab at 20 keV. The Crab ratio exhibits a nearly constant logarithmic slope of ~ 0.5 in the 2–100 keV range. Considering that the Crab spectrum can be approximated by a power law with a photon index of $\Gamma \sim 2.1$, this implies that the spectrum of GRO J1655–40 also takes a power-law shape, but with $\Gamma \sim 1.6$. We hence conclude that GRO J1655–40 was in the low/hard state during the Suzaku observation. In detail, the slope in the 10–70 keV band is slightly harder than that in 3–10 keV. The strong drop in the Crab ratio below 1 keV is caused by a higher absorbing column density toward GRO J1655–40 than that to the Crab.

At energies above ~ 100 keV, the Crab ratio in figure 4 exhibits a clear turnover. Since the Crab spectrum, which is about an order of magnitude brighter than that of GRO J1655–40 at ~ 100 keV, is known to exhibit a single power-law shape in the hard X-ray range up to 300 keV or more (e.g., Kuiper et al. 2001), the hint of a turnover in the Crab ratio suggests an intrinsic high-energy cutoff in the GRO J1655–40 spectrum, as is often observed from other BHBs in the low/hard state. In the figure, the ratios are also plotted by artificially changing the GSO background intensity by $\pm 2\%$, which is the typical error as described in the Appendix. Thus,

the presence of a turnover itself is unaffected by the GSO background uncertainty, although the steepness of the cutoff might be affected.

3.3. Light Curves

Figure 5 shows background-subtracted light curves of GRO J1655–40 obtained with the XIS and HXD-PIN. The intensity decreased gradually during this one-day long observation, by $\sim 35\%$ in the softest 0.7–2 keV band and by $\sim 25\%$ in the higher energy bands, resulting in a slight spectral hardening with time.

In order to quantify the intensity-correlated spectral changes, we divided the data into two halves, which we hereafter refer to as the first and second halves (figure 5). We then extracted the corresponding energy spectra from the XIS and PIN. (As mentioned above, we did not attempt such time-resolved spectral analysis on the GSO data.) The time coverage was half a day for each of the first and second halves of the PIN data, and the blank-sky PIN background was accumulated over the corresponding portions of the BD+30°3639 observation.

Figure 6 shows spectral ratios between the two halves. The source intensity decreased by $\sim 10\%$ above ~ 3 keV, and by up to $\sim 18\%$ below ~ 3 keV. Thus, the intensity decrease is somewhat more prominent at low energies, in agreement with the impression from the light curves. (These percentages are smaller than are indicated by the light curves, simply because of time averaging effects.) This suggests the presence of a separate soft spectral component, which is superposed on the dominant power-law shaped continuum that is emitted over the entire energy band.

3.4. Spectral Model Fitting

3.4.1. The XIS spectra

As a first-cut quantitative spectral study, we tried an absorbed single power-law model on the XIS data of GRO J1655–40, as suggested by the Crab ratio in figure 4. Specifically, we fitted the spectrum from the BI-CCD (XIS1) and that from the two FI-CCDs (XIS2 and XIS3 co-added) simultaneously, using the detector responses `ae_xi1_20060213c.rmf` and `ae_xi1_xisnom4_20060415.arf` for XIS1, and averages of `ae_xi[23]_20060213.rmf` and `ae_xi[23]_xisnom4_20060415.arf` for the co-added FI spectrum. Here and hereafter, fits to the XIS spectra utilize only the 0.7–1.7 keV and 1.9–8 keV ranges, because the excluded energy bands are still subject to calibration uncertainties or possible pile-up effects. The effect of contamination on the optical blocking filters of the XIS is modeled as additional absorption (Koyama et al. 2007). In the fitting, we kept the energy offset to be a free parameter within ± 10 eV, which is the current tolerance of the XIS energy scale. The overall model normalization is here and hereafter allowed to differ between different XIS sensors.

The single power-law fit, with a free photon index Γ and a free absorbing column density N_{H} (using the “wabs” model; Morrison & McCammon 1983), was formally rejected by the XIS data with $\chi^2/\nu = 1924/1424$, mainly due to wiggling residuals at energies below ~ 1.5 keV.

This, together with the soft-energy behavior revealed by figure 6, inspired us to incorporate an independent soft component. Evidently, the most natural candidate is an optically-thick disk emission component which is described by the “disk-blackbody (diskbb)” model (Mitsuda et al. 1984; Makishima et al. 1986). We therefore adopted a model consisting of a power-law and a disk blackbody, both absorbed by a common absorber with column density N_{H} . This composite model, denoted by “diskbb+pow”, gave a much improved fit with $\chi^2/\nu = 1738/1422$, yielding an innermost disk temperature of $kT_{\text{in}} \sim 0.26$ keV and an innermost disk radius of $r_{\text{in}} \sim 10/\sqrt{\cos(i)}$ km at a distance of 3.2 kpc, where i is the inclination angle of the disk. Nevertheless, the model was not yet fully acceptable, because of some positive residuals in the 5–8 keV energy range.

Finally, we obtained $\chi^2/\nu = 1499/1419$, by adding a broad ($\sigma = 1.04_{-0.10}^{+0.13}$ keV) Gaussian line component, centered at $E_{\text{center}} = 6.50 \pm 0.08$ keV and having an equivalent width (EW) of 280 ± 40 eV. The fit is in fact marginally unacceptable at the 99% confidence level, but the fit statistic has a similar value to that obtained when we fit the Crab spectrum with an absorbed single power-law model. Thus, we considered that this fitting is essentially acceptable under the current level of instrumental calibration and response adjustments. Although we cannot rule out the possibility of this Gaussian feature having an instrumental origin, the obtained Gaussian parameters are suggestive of a broad iron line, or some related spectral features. The obtained best-fit parameters are listed in table 1. The power-law component has $\Gamma = 1.75$, which is typical of an accreting black hole in the low/hard state. The “diskbb” component has an innermost disk temperature of 0.18 keV, and carries 10.2% of the 0.5–2 keV source flux (or 4.1% in the 0.5–10 keV range).

We used numerical modeling (Koyama et al. 2007) to represent the effects of contamination on the optical blocking filters of the XIS sensors. The model, which is still under development, may include some unknown systematic errors. However, this should not affect our results significantly, since the contaminant was not so thick when the present observation was performed (only two months after the launch). Also, we did not use data below energies of 0.7 keV, since there is a relatively high interstellar column density toward GRO J1655–40.

3.4.2. The HXD spectra

Before actually conducting model fitting to the HXD-PIN and GSO spectra of GRO J1655–40, we briefly describe the HXD data of the Crab Nebula. With the current PIN response (ae_hxd_pinxiom_20060814.rsp), the 10–70 keV PIN spectrum of the Crab Nebula can be successfully represented by a single power-law model with $\Gamma = 2.09 \pm 0.01$, which agrees with numerous previous measurements. Similarly, using the GSO response ae_hxd_gsoxiom_20060321.rsp, the 100–300 keV GSO spectrum of the Crab is reproduced to a reasonable accuracy with $\Gamma \sim 2.1$ (Kokubun et al. 2007).

Strictly speaking, the single power-law fit to the GSO spectrum of the Crab over the 70–300 keV range, using the current GSO response, is formally unacceptable, due to mild ($\sim 10\%$) convex residuals [see figure 18 in Kokubun et al. (2007)]. This implies that the GSO response

predicts spectra that are slightly too concave than it should. Therefore, the GSO response needs to be improved, or at least corrected, when we try to quantify the high-energy cutoff of GRO J1655–40 suggested by its Crab ratio. In order to make the necessary correction in an explicit manner, we have resorted to introducing an empirical correction factor of the form

$$C(E) \equiv 1.36 (E/100)^{0.65} \exp(-E/230) \quad , \quad (1)$$

where E is the energy in keV, and multiplying this factor to any input model before it is convolved with the current GSO response. This function, $C(E)$, has a mildly convex shape with a peak at ~ 150 keV, and takes values in the range $0.75 - 0.93$ for $70 < E < 300$. In fact, this particular functional form has been determined so that the current GSO response can successfully reproduce the 70–300 keV spectrum of the Crab Nebula by a single power-law with $\Gamma = 2.1 \pm 0.1$, when the input power-law model is multiplied by $C(E)$. Hereafter in the present paper, we always include this factor $C(E)$ when fitting GSO spectra.

With these preparations, we fitted the HXD (PIN and GSO) spectra of GRO J1655–40, after subtracting the BD+30°3639 spectra as the blank-sky backgrounds (subsection 3.1). A single power-law model (but multiplied by equation (1) when simulating the GSO data) failed to give an acceptable joint fit to the PIN and GSO spectra, with $\chi^2/\nu = 145/68$, even though the relative PIN versus GSO normalization was left free to vary. Since the model was actually over-predicting the GSO data above 100 keV, we replaced the power-law model with a cut-off power-law (hereafter “cutoffpl”) model, namely, a power-law multiplied by an exponential factor of the form $\exp(-E/kT_{\text{cut}})$, where k is the Boltzmann constant and T_{cut} is the cutoff “temperature”. This model gave an acceptable ($\chi^2/\nu = 64/67$) joint fit to the PIN and GSO spectra of GRO J1655–40, with the relative PIN versus GSO normalization in agreement within 10% of that obtained from the Crab analysis. The best-fit parameters are listed in table 1, including in particular values of $\Gamma = 1.35 \pm 0.04 \pm 0.05$ and $kT_{\text{cut}} = 200_{-30, -60}^{+50, +140}$ keV, where the first errors are statistical and the second ones reflect the 2% systematic uncertainty in the GSO background subtraction. The systematic errors may be somewhat overestimated, because the value of 2% is rather conservative (see Appendix).

By means of model fitting to the HXD data, we have thus confirmed quantitatively the presence of the high-energy spectral turnover which is suggested by the Crab ratio. Although the upper bound on kT_{cut} is rather loose when considering the GSO systematics, an F -test indicates that the data still prefer the “cutoffpl” model to the single power-law model, because the probability of the cutoff being insignificant is 4×10^{-7} , even if we adopt the worst case of 2% under estimation of the background. If the correction factor described by equation (1) is not incorporated, the requirement of the high energy cutoff by the HXD data for GRO J1655–40 is even stronger.

With $kT_{\text{cut}} \sim 200$ keV, the “cutoffpl” model as determined above from the HXD data implies a slope of $\Gamma \sim 1.35$ in the 1–10 keV range. This is smaller by ~ 0.4 than that determined

by the XIS (§ 3.4.1). This reconfirms the inference obtained by inspecting the Crab ratio (§ 3.2, figure 4), that HXD-PIN measures a flatter slope than the XIS.

As a consistency check, we repeated the same analysis using the HXD data, except that the model background was subtracted (§ 3.1) instead of the blank-sky data. The obtained parameters from this analysis are $\Gamma = 1.39 \pm 0.04$ and $kT_{\text{cut}} = 290_{-60}^{+100}$ keV. As expected from the good agreement between the two sets of backgrounds (figure 2), neither the goodness of fit nor the best-fit parameters differ significantly between the two methods, reinforcing the reality of the high-energy cutoff.

3.4.3. Broad-band spectra

Following the above analysis, we next jointly fitted the time-averaged XIS and HXD (PIN and GSO) spectra. Although it would be natural to employ a model consisting of “diskbb” and “cutoffpl” components, here a more physically consistent approach may be adopted. Since the hard X-ray emission from BHBs in the low/hard state is generally interpreted as resulting from thermal Comptonization of some soft photons by hot electrons with a temperature kT_e (§ 1), we decided to represent the hard continuum with “compps” model (Poutanen & Svensson 1996) in xspec, instead of the “cutoffpl” model. The “compps” code computes Compton scattering in an exact manner incorporating the Klein-Nishina effect, and is known to accurately reproduce the Wien peak particularly when the electron temperature is high.

Our new fitting model thus becomes “diskbb+compps+gau”, where the broad Gaussian component around 6 keV (§ 3.4.1) is retained with its parameters left free. Because the “compps” code allows us to use an optically-thick disk emission as a seed photon source generated at the center of the hot plasma, we substitute the “diskbb” temperature for this seed-photon temperature. Then, the “compps” normalization, equivalent to the seed photon flux, becomes proportional to the square of innermost radius $r_{\text{in}}^{\text{comp}}$ of the assumed seed disk, although this parameter, $r_{\text{in}}^{\text{comp}}$, can differ from the original r_{in} . The implied picture is that a fraction $[\propto (r_{\text{in}})^2]$ of photons from a disk-blackbody source is directly observed as the soft excess, while the rest $[\propto (r_{\text{in}}^{\text{comp}})^2]$ is injected into the Comptonizing plasma. With the seed photon source thus specified, the “compps” model has two basic free parameters: one is kT_e , and the other is so-called Compton y -parameter which is related to the optical depth τ by

$$y \equiv 4\tau \frac{kT_e}{m_e c^2} \quad , \quad (2)$$

where $m_e c^2$ is the electron rest mass energy. Among several available geometries provided by “compps”, we chose a sphere (parameter=4), so as to make the Comptonized spectrum independent of the inclination.

We thus fitted this “diskbb+compps+gau” model jointly to the XIS, HXD-PIN, and HXD-GSO spectra, again incorporating equation (1) for the GSO data. The overall model normalization was allowed to take different values between the XIS and HXD-PIN, to “absorb” residual calibration uncertainties. In contrast, considering the results obtained in section 3.4.2,

and the fact that the GSO scintillators are placed directly behind the PIN diodes, we constrained the PIN versus GSO normalization to stay within $\pm 10\%$ of the nominal value determined from the Crab spectra. This tolerance reflects the systematic GSO background uncertainty of $\pm 2\%$ (see Appendix), which amounts to $\sim \pm 10\%$ of the source flux in the PIN/GSO overlapping energy range. Hereafter in this section, we show only the results using the blank-sky background, since the modeled background yields consistent results.

As presented in figure 3b, this “diskbb+compps+gau” model provided a rather poor joint fit to the three spectra, with $\chi^2/\nu = 2408/1489$ (table 2). This is because the fit residuals for the PIN and GSO data are seen to rise toward higher energies, yielding $\chi^2/\nu = 576/70$ if the jointly determined model is compared with the HXD data only. This again implies that the continuum slope above 10 keV is harder than that in the XIS band, as found previously with the Crab ratio and from the separate model-fitting of the XIS ($\Gamma = 1.75$) and the HXD ($\Gamma = 1.35$) spectra. Although the fit is unacceptable, the electron temperature obtained is $kT_e \sim 60$ keV, implying a cutoff energy of $3kT_e \sim 180$ keV (since the optical thickness of the “compps” is rather large), which is consistent with kT_{cut} derived from the HXD data using the “cutoffpl” model. The “diskbb” parameters became different from those derived using the XIS data only, because we replaced the power-law with a “compps” model.

The failure of the above fit suggests the presence of a hard spectral hump, due to reflection from thick matter (e.g., Lightman & White 1988; Ebisawa et al. 1996). We therefore activated an option in the “compps” model, to include reflection of the Comptonization continuum by a thin disk. We set free three parameters specifying the reflector; the solid angle $\Omega/2\pi$ viewed from the photon source, its photo-ionization parameter ξ in units of erg cm s^{-1} , and its inner radius R_{in} in units of R_s where R_s is Schwarzschild radius. The reflector was assumed to have an outer radius of $1000 R_s$, and a radial emissivity profile of $\propto r^{-q}$, where r is the radius and $q = 3$ is emissivity index (Fabian et al. 1989). The remaining reflector parameters, namely the inclination angle, abundance, and temperature, were fixed at 70° , 1 solar, and 10^6 K, respectively. The broad Gaussian line around 5–8 keV is included keeping the parameters free, which is here interpreted as an iron fluorescent line associated with the reflection emission. As shown in figure 3c and table 2, this “diskbb+compps+reflection+gau” model favored $\xi \sim 0$ to represent the hard spectra in the HXD band. However, the fit was not improved significantly, with $\chi^2/\nu = 2246/1486$ (0.7–300 keV) and $484/70$ (10–300 keV). The hard excess still remained above ~ 50 keV because the reflection hump cannot become hard enough above several tens of keV.

To better reproduce the broad-band spectrum, the model must predict a harder and slightly concave continuum. Therefore, as in Frontera et al. (2001), we included an additional “compps” component, instead of the reflection component. The two “compps” components were assumed to share the same kT_e , but were allowed to have independent values of y . As shown in figure 3d and table 2, this “diskbb+compps+compps+gau” model has improved the

fit to $\chi^2/\nu = 1600/1487$ and $85/70$ in the total (0.7–300 keV) and the HXD (10–300 keV) band, respectively. With the electron temperature of ~ 55 keV, the obtained Compton y -parameters, ~ 0.5 and ~ 1.3 , translate to optical depths of ~ 1.2 and ~ 3.0 , respectively. The Gaussian component has an equivalent width of ~ 110 eV. The above two-“compps” model requires a broad Gaussian, which is generally considered to be an indication of a reflection component. Therefore, we further modified the model, assuming that the two “compps” components are both accompanied by reflection with a common set of reflection parameters. The obtained parameters are listed in table 2, and the residuals from the best fit model are shown in figure 3 e. This “diskbb+compps+compps+reflection+gau” model gave $\chi^2/\nu = 1524/1484$ (0.7–300 keV) and $67/70$ (10–300 keV). Thus, the inclusion of the reflection component has significantly improved the fit, and makes it acceptable at the 90% confidence limit. Also this reflection component may naturally explain the Gaussian component. Therefore, we adopt this model in the following part of this paper. The Compton y -parameters, ~ 0.28 and ~ 1.3 , are almost the same as those from the “diskbb+compps+compps+gau” fit, but the obtained $kT_e \sim 140$ keV is twice as high, thus halving the optical depths to ~ 0.25 and ~ 1.2 respectively. As shown in figure 7, this fit implies a relatively strong reflection component with $\Omega/2\pi = 0.6 \pm 0.1$. This makes kT_e higher, because the spectral cutoff above ~ 100 keV is partially explained away by the turn-over intrinsic to the reflection component.

3.4.4. Changes in the broad-band spectra

Following the above analysis that was based on data averaged over the whole observation time, we applied the same “diskbb+compps+compps+reflection+gau” model separately to the first-half and second-half spectra, obtained in § 3.3 by the XIS and HXD-PIN. (As noted before, we did not split the GSO data into the two halves, and the PIN data refer to those using the blank-sky background only.) The reflection parameters (Ω , ξ and R_{in}) were fixed to the best-fit values of the average spectrum (table 2). As summarized in table 3, this model has successfully reproduced both spectra. As the 0.7–300 keV source luminosity decreased by 10%, the two Compton y -parameters stayed nearly constant, while kT_e increased marginally. The additional 8% decrease (total $\sim 18\%$) fractional decrease of the flux below 3 keV (figure 6) is driven solely by a decrease in the diskbb component, although the error of the luminosity of the disk component is large.

3.5. Narrow Iron Line Structure

Although the XIS data might be consistent with the presence of a broad ($\sigma \sim 1.0$ keV) iron line feature (§ 3.4.1), much narrower emission/absorption lines are often observed from BHBS. We therefore searched the XIS spectra for relatively narrow iron K absorption or emission features. Figure 8 shows an expanded view of the 5–8 keV portion of the XIS spectra, where a power-law model with a broad Gaussian mentioned in §3.4.1 was fitted to the data over this limited energy range. As is evident from the fit residuals plotted in the bottom panel of

figure 8, no narrow spectral features are present. We added another Gaussian line to the model, allowing its normalization to have both positive and negative values. By fixing the centroid energy of the added Gaussian at various trial values between 6.0 and 7.0 keV, we determined the allowed regions of its Gaussian equivalent width EW. The results are shown in figure 9, where three cases of the Gaussian intrinsic width were examined: 1 eV, 100 eV, and 200 eV in the Gaussian standard deviation, based on the reports by Sala et al. (2007) (~ 110 eV, ~ 200 eV, and ~ 250 eV) and Diaz Trigo et al. (2007) (~ 100 eV). The allowed EWs of positive (emission line) and negative (absorption line) features, at the 90% confidence level, are less than 20 eV and 23 eV, respectively, for an intrinsic width of 200 eV. If we consider the energy range above 6.4 keV, the upper limits of the EW are ~ 20 eV and ~ 15 eV for the emission and the absorption features, respectively.

4. Discussion

We have presented high-quality broad-band (0.7–300 keV) energy spectra of the black hole candidate GRO J1655–40, obtained with Suzaku in a decay phase of the 2005 outburst. Employing the distance of 3.2 kpc and assuming isotropic emission, the 0.7–300 keV luminosity at the time of our observation (estimated using the “diskbb+compps+compps+reflection+gau” model) becomes $\sim 5.1 \times 10^{36}$ erg s $^{-1}$, equivalent to $\sim 0.7\%$ of L_E for a 6 M_\odot black hole. The spectra are dominated by a power-law like continuum, implying that the object was in a typical low/hard state. The continuum is approximated by a photon index of ~ 1.75 and ~ 1.35 at energies below and above ~ 10 keV, respectively, together with a high-energy cutoff around an energy of ~ 200 keV. The spectra do not exhibit narrow iron emission or absorption lines in the 5–8 keV band, but they do show a weak soft excess. The continuum cannot be reproduced by a single thermal Compton model with disk reflection, but can be explained successfully by two thermal-Comptonization components having a common kT_e and different optical depths, both accompanied by reflection with $\Omega/2\pi \sim 0.6$. Below, we discuss these spectral characteristics.

4.1. The High Energy Cutoff & Two Comptonization Components

Thanks to the high capability of Suzaku, we have shown that the high-energy spectrum of GRO J1655–40 gradually deviates above ~ 100 keV from a single power-law, exhibiting a high-energy cutoff effect that can be represented by an exponential factor with $kT_{\text{cut}} \sim 200$ keV (or > 110 keV, if we include a maximum systematic error). This reconfirms the RXTE and INTEGRAL detection of a similar effect with $kT_{\text{cut}} \sim 180$ keV, that was made in an early stage of the same outburst (Shaposhnikov et al. 2007). At that time the object was also in the low/hard state, with a similar luminosity of $\sim 4 \times 10^{36}$ erg s $^{-1}$. These two independent observations firmly establish the presence of a high-energy cutoff in the low/hard state spectrum of GRO J1655–40.

Although the presence of a high-energy cutoff supports the thermal Compton scenario,

the observed 3–80 keV continuum exhibits a concave shape in a log-log plot, in contradiction to a prediction of a simple Comptonization scenario that the continuum should have a constant logarithmic slope at energies $\ll kT_e$. The discrepancy cannot be attributed to reflection by cold or partially ionized material, since it can produce a concave curvature only up to ~ 50 keV. Instead, two thermal-Comptonization components (both modeled by “compps”), with different Compton y -parameters, have successfully explained the 0.7–300 keV spectra over the entire energy band (except for the subtle soft excess). As shown in figure 7, the flatter continuum in the HXD-PIN band is explained by the component with the larger Compton y -parameter ($y \equiv y_L \sim 1.3$) that has a flatter photon index of ~ 1.4 , whereas the continuum steepening by $\Delta\Gamma \sim 0.4$ in the XIS band is explained by the addition of the component with the smaller Compton y -parameter ($y \equiv y_S \sim 0.28$) that has a steeper photon index of ~ 2.1 . Of course, there remains a possibility that the two values of y are representing more complex, for example continuous, distributions in the y -parameter.

In our double- y modeling, we assumed for simplicity that the two Compton components have the same kT_e . This does not however rule out the possibility that they have different values of kT_e , since the component with smaller y contributes little to the GSO energy range, and hence its high-energy curvature remains poorly constrained.

The empirical modeling with multiple (at least two) Comptonized continuum components allow two alternative physical interpretations. One is a spatial variation, in which an extended seed-photon source is covered by a hot electron cloud for which the optical depth varies with position; the two components differ in their spatial location but arise effectively simultaneously in time. The other is a temporal variation, in which the optical depth of the hot electron cloud varies on short timescales between, for example, two representative values, so that a time-averaged spectrum would be composed of a superposition of the individual components. The true physics may well be a mixture of these two extreme cases. For further elucidation, we need to study intensity-correlated spectral changes on various timescales. For example, according to Negoro et al. (2001), the 1–60 keV spectrum of Cyg X-1 acquired with Ginga softens around the peak of X-ray “shots”, namely rapid X-ray flaring (see also Poutanen & Fabian 1999). This sort of investigation, however, is beyond the scope of the present paper.

4.2. Comparison of the Compton Parameters with Cyg X-1

The existence of two Compton components with different y -parameters was previously reported from Cyg X-1 in a low/hard state observed with BeppoSAX (Frontera et al. 2001), when the 0.5–200 keV luminosity was $\sim 2.0 \times 10^{37}$ erg s $^{-1}$. Employing the same “compps” modeling, these authors measured the Compton parameters of Cyg X-1 as $y_S \sim 0.15$ and $y_L \sim 0.89$, together with $kT_e \sim 60$ keV. The implied optical depths are ~ 0.5 and ~ 1.9 . Thus, the double- y modeling has been successful on both these objects, and has yielded roughly similar sets of spectral parameters except for minor differences.

Compared with these values for Cyg X-1, the two y -parameters of GRO J1655–40 observed with Suzaku, particularly y_L , are considerably larger. This is a direct consequence of the fact that the BeppoSAX spectrum of Cyg X-1 is steeper than that of GRO J1655–40 obtained with Suzaku. The difference in y can be attributed to the higher electron temperature of GRO J1655–40 (140 keV), than that of Cyg X-1 observed with BeppoSAX (60 keV). This difference in kT_e , in turn, may arise because Cyg X-1 was by a factor of 4 more luminous than GRO 1655–40. In fact, it has been observed in other BHBs (e.g., Esin et al. 1998; Yamaoka et al. 2005) that kT_e decreases with the increasing luminosity, presumably due to the enhanced coronal cooling. This tendency, though marginal, is visible even between the two halves of the present data of GRO 1655–40. However, this mechanism alone may not be sufficient to produce the observed temperature difference, since the two objects are implied to have relatively similar luminosities when normalized to their Eddington luminosity, given the mass of $\sim 6 M_\odot$ of GRO J1655–40 and $\sim 20 M_\odot$ of Cyg X-1 (Ziolkowski 2005).

In spite of the rather extreme edge-on inclination, GRO J1655–40 are inferred to have comparable, or even smaller, Compton optical depths (1.2 and 0.25, if we adopt $kT_e \sim 140$ keV for both the Comptonizing clouds.) than Cyg X-1 (1.9 and 0.5). This would not happen if the Comptonizing cloud had an oblate geometry extending along the disk plane. Therefore, the relation between the two objects is consistent with the generally accepted view that the Comptonizing cloud has a relatively large scale height perpendicular to the disk plane, so that the emergent hard X-rays are approximately isotropic.

We have so far ascribed the spectral difference between GRO J1655–40 and Cyg X-1 to their differences either in the inclination angles or in the luminosities. In reality, both these effects can be operating, that would cause GRO J1655–40 to have larger y -parameters. Although this subject is important in constructing a unified picture of BHBs in the low/hard state, further examination of it is beyond the scope of the present paper.

4.3. *The Seed Photons and Soft Excess*

In the present analysis, we have assumed that the two “compps” (Comptonized continuum) components are both supplied with seed photons by “diskbb” sources that have a common kT_{in} . Taking a quadratic sum of the two “compps” normalizations (table 2), the innermost disk radius of the seed photon source is obtained as $r_{\text{in}}^{\text{comp}} \sim 56/\sqrt{\cos(i)}$ km.

The XIS spectra require an additional soft-excess component to be added to the power-law continuum (§ 3.4.1). We also expressed it in terms of a simple “diskbb” model, and required it to have the same innermost temperature as the seed photon disk. This modeling has yielded $r_{\text{in}} \sim 17_{-17}^{+8}/\sqrt{\cos(i)}$ km together with $kT_{\text{in}} \sim 0.18$ keV. (Although this error region of r_{in} includes no-“diskbb” assumption, the spectrum of the first half (table 3) requires significant “diskbb” component.) Therefore, based on the assumption made in § 3.4.3, substantial part of the cool accretion disk is thought to be covered by the Comptonizing cloud, while the remaining part

$[\propto (r_{\text{in}})^2]$ is directly visible as the soft excess. The overall innermost radius then becomes $\sim 59/\sqrt{\cos(i)}$ km, as a quadrature sum of $r_{\text{in}}^{\text{comp}}$ and r_{in} . Assuming an inclination angle of $i = 70^\circ$ (van der Hooft et al. 1998), the physical size of the innermost disk radius becomes ~ 100 km, or $\sim 6 R_s$ for a black hole of $6M_\odot$ (Shahbaz et al. 1999). The estimated disk radius is a factor of 4–7 larger than the values inferred from observations of this object in the high/soft state (Sala et al. 2007; Kubota et al. 2001).

As argued so far, the “diskbb” interpretation of the soft excess leads to a view that the optically-thick disk has retreated outwards, by up to an order of magnitude in radius, compared to its location during the high/soft state. This is consistent with the general picture regarding the relation between these two states. Nevertheless, the estimated inner radius of the cool disk is small enough to suggest that a considerable fraction of seed photons to the Comptonization process is provided by the inner region of the cool disk which is immersed in the hot corona. Then, the Compton cloud would be cooled by its own radiation, which are intercepted by the cool disk, reprocessed there, and re-emitted into the cloud. In such a case, the photon index of the Comptonized component is expected to become $\Gamma \sim 2$ (Haardt & Maraschi 1993), though depending on the ratio of energy inputs to the disk and the hot cloud (Gilfanov et al. 2004). Since we observed a much flatter continuum ($\Gamma \sim 1.4$), some modification to the scenario might be needed (e.g., Beloborodov 1999).

Although the “diskbb” modeling of the soft excess gives a natural and self-consistent interpretation, it may be explained in alternative ways. For example, the excess may result from scattering of the soft part of the continuum by interstellar dust grains. Actually, Greiner et al. (1995) detected a dust scattering halo around GRO J1655–40, and Sala et al. (2007) reported changes in the intensity of the scattered component in 24 hours. Yet another possibility is that the soft excess is intrinsic to the hard continuum itself, and produced, for example, by the “shots” mentioned in the previous section (§ 4.1). Then, the observed change in the soft excess intensity could be attributed to variations in the average shot rate.

4.4. *Iron Line Features*

The broad emission structure at 5–8 keV has an equivalent width of ~ 80 eV, when modeled with “diskbb+compps+compps+reflection+gau”. The reflection component in the “compps” model does not include Fe-K line emission so the broad feature in the data is being modeled by both the complexity in the reflection component and the fluorescent iron lines, presumably smeared by the disk motion.

In previous observations of GRO J1655–40 made in the high/soft state, narrow Fe-K absorption lines were detected repeatedly, with equivalent widths of, for example, 61_{-13}^{+15} eV (Ueda et al. 1998), 60–110 eV (Sala et al. 2007), and 60–80 eV (Fe XXV+Fe XXVI; Diaz Trigo et al. 2007). In contrast, the present Suzaku observation conducted in the low/hard state has shown that any such feature has to have an equivalent width < 25 eV, which is considerably

smaller than values observed in the high/soft state. The present upper limit on the Fe XXV $K\alpha$ line equivalent width constrains the column density of the corresponding ions to $< 10^{19}$ cm^{-2} from a curve of growth (Ueda et al. 1998), assuming that the absorbing plasma has a temperature of 0.1 keV. This value is more than an order of magnitude lower than that estimated in the high/soft state. Further, considering that the detections of Fe-K absorption line features from BHBs (including GRO J1655–40 itself) have all been achieved in the high/soft state, the present non-detection can be most naturally attributed to the fact that the source was in the low/hard state.

In the high/soft state, the Fe-K absorption features are considered to be formed by a highly ionized absorber, that is located at a distance of $(5-10) \times 10^9$ cm (Sala et al. 2007; Ueda et al. 1998), or $\sim 5 \times 10^8$ cm (Miller et al. 2006b) from the central black hole. It is suggested that such a line-forming absorber, present in the high/soft state, undergoes significant geometrical and/or physical changes when the system makes a transition into the low/hard state. Then, the absorber may become either fully ionized from illumination by the intense X-rays, or too tenuous (for unknown reasons), or too turbulent, so that the formed line features are smeared out.

Acknowledgment

We thank Drs. Andrzej A. Zdziarski and Chris Done for useful comments on the thermal-Comptonization models. We acknowledge that a part of this work is supported by the project of the Research Center of the Advanced Measurement at Rikkyo University, and the Grant-in-Aid for Specially Promoted Research (Grant No. 14079101). S.K. gratefully acknowledges the financial support of the Grant-in-Aid for Scientific Research (Grant No. 14654039 and No. 15037208). SN acknowledges the support by JSPS (Japan Society for the Promotion of Science) post doctoral fellowship for foreign researchers (P05249).

Appendix. HXD Background Subtraction with Blank-Sky Observations

To detect signals from faint sources, reliable background subtraction from observed data is essential. Compared with previous instruments, the HXD has a factor of several times lower background level with efficient background-subtraction systems and can achieve a higher sensitivity, even though the background has an uncertainty of $\sim 5\%$ (Takahashi et al. 2007). Since the HXD does not have capabilities of imaging or rocking of the detector to observe source-free regions, we need to estimate the background using a background model (Kokubun et al. 2007). In the current analysis, we used two types of background for subtraction. Namely, that from a blank-sky observation and that from modeled background, since our data analysis was begun before the modeled background was available. Thus, we examine here the systematic error of the former background-subtraction method, namely using data from the observation of BD+30°3639 made one day before that of GRO J1655–40, based on the investigation of Kokubun et al. (2007). The latter subtraction method, using a background model, has been developed by the HXD instrument team ² and the detailed properties of the modeling are described in another paper.

As described in § 3.1, the source flux of GRO J1655–40 is so high that the systematic error of the PIN background is considered to be negligible. On the other hand, since the background of the GSO detector is higher than that of the PIN, and the flux from celestial objects becomes fainter in the higher energy band, the source signal of GRO J1655–40 is 25% and 10% of the background flux in the 40–100 keV and 100–300 keV bands, respectively. Thus, we describe the systematic error of the GSO background averaged over one day in the present GRO J1655–40 analysis, by dividing the background into some components and studying the variation of each component. Note that the flux of the Cosmic X-ray background is 2-3 orders of magnitude smaller than that of the GSO background, and it is negligible.

There are five components that affect the estimate of the GSO background spectrum in the GRO J1655-40 analysis (Kokubun et al. 2007): (1) a component with a constant flux, namely natural radioactive isotopes included in the detector; (2–4) components from radio-activated sources that are accumulated through the passages of the South Atlantic Anomaly (SAA) and have half-lives longer than a day [denoted as “long-nuclides” in Kokubun et al. (2007)], from ~ 100 min to a day (“middle-nuclides”), and of $\lesssim 100$ min (“short-nuclides”), and (5) a component that changes in magnitude due to the flux of cosmic-ray particles, depending on the Cut-Off Rigidity (COR).

Although component (1) constituted $\sim 10\%$ of the total background flux on 2005 September 22 (Kokubun et al. 2007), its spectrum has already been measured during ground calibration and is temporally stable (Takahashi et al. 2007). Therefore, there is a very small systematic error ($\lesssim 0.1\%$) in the total background flux induced in the background by component

² <http://www.astro.isas.jaxa.jp/suzaku/analysis/hxd/hxdnxb/>

(1).

In the case of component (2), the growth curves of both line and continuum components have been well-studied by Kokubun et al. (2007). Although the line components at 70 and 150 keV are the ones that grow most significantly, their half-lives are ~ 240 days and the difference between adjacent days is only $\exp(1/240) \sim 0.3\%/day$.

The flux of component (3) changes moderately on a timescale of days, reflecting the number of high energy particles irradiated during SAA passages. The number is counted by the PIN upper-discriminator (UD) counter even during the SAA (Takahashi et al. 2007), and has a 50-day cycle that comes from the orbital modulation between the spacecraft and the SAA (Kokubun et al. 2007). Figure 21 of Kokubun et al. (2007) shows that the PIN UD amplitude of the 50-day cycle is $\sim 30\%$ (65 ± 10 counts s^{-1}), and we can estimate that the systematic error of the background caused by component (3) is $0.3 / (50/2 \text{ days}) \sim 1.2\%/day$. The observation time of GRO J1655–40 (2005 September 22) corresponds to a declining phase of the modulation (Kokubun et al. 2007), and the background is over-subtracted by $\sim 1.2\%$ when that background was obtained from the BD+30°3639 observation, which was taken one day before the GRO J1655–40 observation.

The light curve of the blank-sky background observation (BD+30°3639) is shown in figure 10 in two different energy bands, 40–100 keV and 100–300 keV, for which the data processing was the same as that described in § 3.1. The former data, where the flux increases periodically, are from orbits when the satellite went through the SAAs, and the variation is caused by component (4). The background variation in the lower 40–100 keV band is more significant than that in the 100–300 keV band. See Kokubun et al. (2007) for the energy spectrum of component (4). The rate increases by at most a half of the constant flux in the 40–100 keV band over a duration of half a day. Assuming that the shape of the increase in count rate of the background light curve is a triangle over half a day, the additional amounts of the background caused by (4) are obtained as $0.5/2/2 \sim 13\%$ of the constant flux over a one-day period. The flux of component (4) also depends on the number of particles irradiated during each SAA, and the difference between the GRO J1655–40 and BD+30°3639 observations is directly comparable with the PIN-UD counts measured in the two observations, since the half-life of the component (4) is smaller than ~ 100 min. Figure 11 shows the PIN UD rates of the WELL Unit 00 (Takahashi et al. 2007) during the observations of GRO J1655–40 and BD+30°3639. The observed total PIN UD counts are 7.30×10^7 for GRO J1655–40 and 7.70×10^7 for BD+30°3639. The difference is 5%, and the integrated start and stop times of the two datasets were adjusted to overlap each other. Therefore, we can estimate that the systematic error caused by component (4) is $0.13 \times 0.05 \sim 0.7\%$ of the total background count rate in the 40–100 keV band. In the higher 100–300 keV band, the variation amplitude of component (4) is about half of that in the 40–100 keV band, resulting in a systematic error of $\sim 0.4\%$ in the total background flux. Since the distribution of the time after the SAA

passage was adjusted between the two observations as described in § 3.1, it does not affect the systematic error of the background.

The background variation in the latter half of figure 10 is caused by a difference in the COR (Kokubun et al. 2007), and it is considered that component (5) constitutes $\sim 10\%$ and $\sim 5\%$ of the total flux in the background in the 40–100 keV and 100–300 keV energy band respectively. See Kokubun et al. (2007) for details of the COR dependence. Figure 12 compares the COR distributions between the GRO J1655–40 and BD+30°3639 observations. The distributions for the two cases are very similar, with average values of 11.9 and 11.7 GV, respectively. The total of the difference of the exposure time in every COR bin is ~ 600 s, which is $\sim 3\%$ of the total observation time (~ 20 ks). Even if the differences in the background flux for these terms are all 10% of the total background flux in the 40–100 keV band, the systematic error induced by component (5) is considered to be $0.1 \times 0.03 \sim 0.3\%$ of the total background in the 40–100 keV band. Similarly, the error is $0.05 \times 0.03 \sim 0.2\%$ in the 100–300 keV band.

From the above discussion, the systematic errors in the GRO J1655–40 background obtained from the BD+30°3639 dataset are summarized for each component as (1) $\lesssim 0.1\%$, (2) $+0.3\%$, (3) -1.2% , (4) -0.7% over 40–100 keV and -0.4% over 100–300 keV, and (5) at most -0.3% over 40–100 keV and -0.2% over 100–300 keV, where the symbol “+” represents an under-subtraction and the “-” symbol indicates over-subtraction. Therefore, adding up all the components, the total systematic error of the current background is thought to be at most -1.9% and -1.5% in the 40–100 keV and 100–300 keV bands respectively.

In order to confirm this estimation, we additionally examined three sets of GSO backgrounds obtained during two successive days near the GRO J1655–40 observation. Namely, a BD+30°3639 observation on 2005 September 21 and a HESS J1616-508 observation on 2005 September 20, an RX J1713-39 observation on 2005 September 26 and 25, and a continuous observation of the same source on 2005 September 28 and 27. All the datasets were obtained in the same declining phase of the 50-day cycle of the PIN-UD modulation. We extracted the spectra by the same method as in § 3.1, and we also subtracted the background of the previous day from that of the next day. The result shows that the differences between the two observations are all within $-1.9 \sim +1.5\%$ and $-0.9 \sim 0.0\%$ of the count rate in the 40–100 keV and 100–300 keV bands respectively.

Following the estimation and the result, we assume the peak-to-peak systematic error of the one-day average GSO background spectrum obtained from the adjacent dataset is $\pm 2\%$ in the present GRO J1655–40 analysis, although the error in the 100–300 keV band could be smaller by about a half. This 2% background uncertainty results in 8% and 20% systematic errors in the GRO J1655–40 source spectrum in the 40–100 keV and 100–300 keV bands respectively, since the source signal is 25% and 10% respectively of the background flux in these energy bands.

References

- Bailyn, C. D., Orosz, J. A., Girard, T. M., Joglee, S., della Valle, M., Begam, M. C., Fruchter, A. S., Gonzalez, R., Ianna, P. A., Layden, A. C., Martins, D. H., & Smith, M. 1995, *Nature*, 374, 701
- Balucinska-Church, M., Belloni, T., Church, M. J., & Hasinger, G. 1995, *A&A*, 302, L5
- Beloborodov, A. M. 1999, *ApJL*, 510, L123
- Brocksopp, C., McGowan, K. E., Krimm, H., Godet, O., Roming, P., Mason, K. O., Gehrels, N., Still, M., Page, K., Moretti, A., Shrader, C. R., Campana, S., & Kennea, J. 2006, *MNRAS*, 365, 1203
- Diaz Trigo, M., Parmar, A. N., Boirin, L., Mendez, M., & Kaastra, J. S. 2006, *A&A*, 445, 179
- Diaz Trigo, M., Parmar, A. N., Miller, J., Kuulkers, E., & Caballero-Garcia, M. D. 2007, *A&A*, 462, 657
- Ebisawa, K., Ueda, Y., Inoue, H., Tanaka, Y., & White, N. E. 1996, *ApJ*, 467, 419
- Esin, A. A., Narayan, R., Cui, W., Grove, J. E., & Zhang, S. N. 1998, *ApJ*, 505, 854
- Fabian, A. C., Rees, M. J., Stella, L., & White, N. E. 1989, *MNRAS*, 238, 729
- Fender R. P., Belloni, T. M., & Gallo E. 2004, *MNRAS*, 355, 1105
- Foellmi, C., Depagne, E., Dall, T. H., & Mirabel, I. F. 2006, *A&A*, 457, 249
- Frontera, F., Palazzi, E., Zdziarski, A. A., Haardt, F., Perola, G. C., Chiappetti, L., Cusumano, G., Dal Fiume, D., Del Sordo, S., Orlandini, M., Parmar, A. N., Piro, L., Santangelo, A., Segreto, A., Treves, A., & Trifoglio, M. 2001, *ApJ*, 546, 1027
- Fujimoto, R., Mitsuda, K., McCammon, D., Takei, Y., Bauer, M., Ishisaki, Y., Porter, F.S., Yamaguchi, H., Hayashida, K., & Yamasaki Y. 2007, *PASJ*, 59, S133
- Gies, D. R., & Bolton, C. T. 1986, *ApJ*, 304, 371
- Gilfanov, M., Churazov, E., & Revnivtsev, M. 2004, *X-ray Timing 2003: Rossi and Beyond*, 714, 97
- Greiner, J., Predehl, P., & Pohl, M. 1995, *A&A*, 297, L67
- Haardt, F., & Maraschi, L. 1993, *ApJ*, 413, 507
- Hjellming R. M. & Rupen M. P. 1995, *Nature*, 375, 464
- Kokubun, M. et al. 2007, *PASJ*, 59, S53
- Kotani, T., Ebisawa, K., Dotani, T., Inoue, H., Nagase, F., Tanaka, Y., & Ueda, Y. 2000, *ApJ*, 539, 413
- Koyama, K., et al. 2007, *PASJ*, 59, S23
- Kroeger, R. A., Strickman, M. S., Grove, J. E., Kaaret, P., Ford, E., Harmon, B. A., & McConnell, M. 1996, *A&AS*, 120, 117
- Kubota, A., & Makishima, K. 2004, *ApJ*, 601, 428
- Kubota, A., Makishima, K., & Ebisawa, K., 2001, *ApJ*, 560, L147
- Kuiper, L., Hermsen, W., Cusumano, G., Diehl, R., Schonfelder, V., Strong, A., Bennett, K., & McConnell, M. L. 2001, *A&A* 378, 918
- Lightman, A. P., & White T. R. 1988, *ApJ*, 335, 57
- Makishima, K., *Prog. Theor. Phys.*, submitted (2007)
- Makishima, K., Maejima, Y., Mitsuda, K., Bradt, H. V., Remillard, R. A., Tuohy, I. R., Hoshi, R., & Nakagawa, M. 1986, *ApJ*, 308, 635
- Markwardt, C. B., & Swank, J. H. 2005, *The Astronomer's Telegram*, 414, 1
- McClintock, J. E., & Remillard, R. A. 2003, *astro-ph/0306213*

Miller, J., Raymond, J., Fabian, A., Steeghs, D., Homan, J., Reynolds, C., van der Klis, M., & Wijnands, R. 2006, *Nature*, 441, 953

Miniutti, G. et al. 2007, *PASJ*, 59, S315

Mirabel, I. F., & Rodriguez, L. F. 1994, *Nature*, 371,46

Mitsuda, K., et al. 2007, *PASJ*, 59, S1

Mitsuda, K, Inoue, H., Koyama, K., Makishima, K., Matsuoka, M., Ogawara, Y., Suzuki, K., Tanaka, Y., Shibazaki, N., & Hirano, T. 1984, *PASJ*, 36, 741

Morrison, R., & McCammon, D. 1983, *ApJ*, 270 119

Negoro, H., Kitamoto, S., & Mineshige, S. 2001, *ApJ*, 554, 528

Ninkov, Z., Walker, G. A. H., & Yang, S. 1987, *ApJ*, 321, 425

Poutanen, J. & Fabian, A.C. 1999, *MNRAS*, 306, L31

Poutanen, J. & Svensson, R. 1996, *ApJ*, 470, 249

Quadrelli, A., Malizia, A., Bassani, L., & Malaguti, G. 2003, *A&A*, 411, 77

Reeves, J., et al. 2007, *PASJ*, 59, S301

Risaliti, G. 2002, *A&A*, 386, 379

Sala, G., Greiner, J., Vink, J., Haberl, F., Kendziorra, E., & Zhang, X. L., 2007, *A&A*, 461, 1049

Serlemitsos, P. et al., 2007, *PASJ*, 59, S9

Shahbaz, T., van der Hooft, F., Casares, J., Charles, P. A. & van Paradijs, J. 1999, *MNRAS*, 306, 89

Shaposhnikov, N., Swank, J., Shrader, C. R., Ruppen, M., Beckmann, V., Markwardt, C. B. & Smith, D. A. 2007, *ApJ*, 655, 434

Sunyaev, R. A., & Titarchuk, L. G. 1980, *A&A*, 86, 121

Takahashi, T. et al. 2007, *PASJ*, 59, S35

Tanaka, Y., & Shibazaki, N. 1996 *ARAA*, 34,607

Ueda, Y., Asai, K., Yamaoka, K., Dotani, T., & Inoue, H. 2001, *ApJ*, 556, L87

Ueda, Y. Inoue, H., Tanaka, Y., Ebisawa, K., Nagase, F., Kotani, T., & Gehrels, N. 1998, *ApJ*, 492, 782

van der Hooft, F., Heemskerck, M. H. M., Alberts, F., & van Paradijs, J. 1998, *A&A*, 329, 538

Yamaoka, K., Ueda, Y., Inoue, H., Nagase, F., Ebisawa, K., Kotani, T., Tanaka, Y., & Zhang, S. N. 2001, *PASJ*, 53, 179

Yamaoka, K., Uzawa, M., Arai, M., Yamazaki, T., & Yoshida, A. 2005, *ChJAAS*, 5, 273

Zdziarski A. A., Johnson W. N., & Magdziarz P., 1996, *MNRAS*, 283, 193

Zhang, S. N., Wilson, C. A., Harmon, B. A., Fishman, G. J., Wilson, R. B., Paciesas, W. S., Scott, M., & Rubin, B. C. 1994, *IAU Circl.*, 6046, 1

Zhang, S. N., Ebisawa, K., Sunyaev, R., Ueda, Y., Harmon, B. A., Sazonov, S., Fishman, G. J., Inoue, H., Paciesas, W. S., & Takahashi, T. 1997, *ApJ*, 479, 381

Ziolkowski, J. 2005, *ChJAAS*, 5, 273

Table 1. Best fit parameters obtained with the average spectra from XIS and HXD data, independently. ^{*},[†],[‡]

Data, Model				
pow / cutoffpl	diskbb	gau	wabs	$\chi^2/\text{d.o.f}$
L_x ^{§,¶}	L_x ^{§,¶}	E_c (keV)	N_H ^L	
Γ	r_{in} (km) ^{¶,#}	σ (keV)		
kT_{cut}	kT_{in} (keV)	$E.W.$ (eV)		
All data (XIS), diskbb+pow+gau				
3.70	0.07	6.50 ± 0.08	$7.4_{-0.1}^{+0.2}$	1499/1419
1.75 ± 0.01	45_{-8}^{+9}	$1.04_{-0.10}^{+0.13}$		
...	0.18 ± 0.01	280 ± 40		
All data (PIN+GSO), cutoffpl				
4.61	64/67
1.35 ± 0.04		
200_{-30}^{+50}		

^{*} Errors refer to 90% confidence limits.

[†] The energy offsets of the XIS spectra are adjusted within ± 10 eV.

[‡] The PIN and GSO background spectra are extracted from the one-day before observation (BD+30°3639).

[§] The luminosities are in the 0.7–300 keV band in the unit of 10^{36} erg s⁻¹.

[¶] The distance of 3.2 kpc is assumed.

^L In the unit of 10^{21} H atoms cm⁻².

[#] The value should be divided by $\sqrt{\cos(i)}$, where i is the inclination of the disk.

Table 2. Best fit parameters obtained with the 0.7–300 keV average spectra (XIS+PIN+GSO) ^{*,†,‡}

Data, Model						
compps (soft)	compps (hard)	diskbb	reflection [§]	gau	wabs	$\chi^2/\text{d.o.f}$
L_x ^{¶,Ⓛ}	L_x ^{¶,Ⓛ}	L_x ^{¶,Ⓛ}	L_x ^{¶,Ⓛ}	E_c (keV)	N_H [#]	
$y, r_{\text{in}}^{\text{comp}}$ (km) ^{Ⓛ,††}	$y, r_{\text{in}}^{\text{comp}}$ (km) ^{Ⓛ,††}	r_{in} (km) ^{Ⓛ,††}	$\Omega/2\pi, R_{\text{in}}$ (R_s)	σ (keV)		
kT_e (keV)	... ^{‡‡}	kT_{in} (keV)	ξ (erg cm s ⁻¹)	$E.W.$ (eV)		
All data, diskbb+compps+gau ^{§§}						
3.86	...	0	...	6.4	5.4	2408/1489
0.9, 94	..., ...	0	..., ...	0.5		
60	...	0.10	...	70		
All data, diskbb+compps+reflection+gau ^{§§}						
3.56	...	0	0.44	6.4	5.5	2246/1486
0.9, 94	..., ...	0	0.4, 6	0.5		
70	...	0.10	0	65		
All data, diskbb+compps+compps+gau						
0.82	4.26	0.06	...	$6.4_{-0.2}^{+0.1}$	$7.2_{-0.3}^{+0.2}$	1600/1487
$0.5 \pm 0.1, 34 \pm 4$	$1.3 \pm 0.1, 18 \pm 2$	40_{-6}^{+4}	..., ...	0.7 ± 0.1		
55 ± 5	...	0.18 ± 0.01	...	110		
All data, diskbb+compps+compps+reflection+gau						
0.79	3.63	0.01	0.07(soft), 0.63(hard)	$6.2_{-0.1}^{+0.2}$	$7.4_{-0.2}^{+0.1}$	1524/1484
$0.28_{-0.05}^{+0.11}, 51_{-5}^{+7}$	$1.3_{-0.1}^{+0.2}, 23 \pm 3$	17_{-17}^{+8}	$0.6 \pm 0.1, > 600$	0.6 ± 0.1		
140_{-10}^{+5}	...	0.18 ± 0.01	350 ± 100	80		

* Errors refer to 90% confidence limits.

† The energy offsets of the XIS spectra are adjusted within ± 10 eV.

‡ The PIN and GSO background spectra are extracted from the one-day before observation (BD+30°3639).

§ The reflection of the both “compps” components with the same parameters for two “compps” model.

¶ The luminosities are in the 0.7–300 keV band in units of 10^{36} erg s⁻¹.

Ⓛ A distance of 3.2 kpc is assumed.

In units of 10^{21} H atoms cm⁻².

†† The values should be divided by $\sqrt{\cos(i)}$, where i is the inclination of the disk.

‡‡ The kT_e values are the same between the two “compps” components.

§§ Errors are not shown because of large χ^2 values.

Table 3. The same as table 2 but using the first-half and second-half spectra (XIS+PIN) ^{*,†,‡}

Data, Model						
compps (soft)	compps (hard)	diskbb	reflection [§]	gau	wabs	$\chi^2/\text{d.o.f}$
L_x ^{¶,Ⓛ}	L_x ^{¶,Ⓛ}	L_x ^{¶,Ⓛ}	L_x ^{¶,Ⓛ}	E_c (keV)	N_H [#]	
$y, r_{\text{in}}^{\text{comp}}$ (km) ^{Ⓛ,††}	$y, r_{\text{in}}^{\text{comp}}$ (km) ^{Ⓛ,††}	r_{in} (km) ^{Ⓛ,††}	$\Omega/2\pi, R_{\text{in}}$ (R_s)	σ (keV)		
kT_e (keV)	... ^{‡‡}	kT_{in} (keV)	ξ (erg cm s ⁻¹)	$E.W.$ (eV)		
First half, diskbb+compps+compps+reflection+gau						
0.90	3.80	0.02	0.10(soft)+0.68(hard)	$6.3^{+0.2}_{-0.1}$	7.4 ± 0.1	808/798
$0.28^{+0.09}_{-0.08}, 55^{+7}_{-6}$	$1.3^{+0.3}_{-0.1}, 23^{+2}_{-3}$	22 ± 8	$0.6^{\text{§§}}, 900^{\text{§§}}$	0.7 ± 0.1		
135^{+5}_{-10}	...	0.18 ± 0.01	$350^{\text{§§}}$	100		
Second half, diskbb+compps+compps+reflection+gau						
1.00	3.27	< 0.02	0.12(soft)+0.60(hard)	6.2 ± 0.1	$7.4^{+0.2}_{-0.1}$	880/924
$0.31^{+0.11}_{-0.05}, 52^{+7}_{-5}$	$1.4^{+0.4}_{-0.1}, 28^{+2}_{-3}$	< 21	$0.6^{\text{§§}}, 900^{\text{§§}}$	0.6 ± 0.1		
155 ± 15	...	0.18 ± 0.01	$350^{\text{§§}}$	90		

* Errors refer to 90% confidence limits.

† The energy offsets of the XIS spectra are adjusted within ± 10 eV.

‡ The PIN background spectra are extracted from the one-day before observation (BD+30°3639).

§ The reflection of the both “compps” components with the same parameters for two “compps” model.

¶ The luminosities are in the 0.7–300 keV band in units of 10^{36} erg s⁻¹.

Ⓛ A distance of 3.2 kpc is assumed.

In units of 10^{21} H atoms cm⁻².

†† The values should be divided by $\sqrt{\cos(i)}$, where i is the inclination of the disk.

‡‡ The kT_e values are the same between the two “compps” components.

§§ Reflection parameters are fixed to those of the average spectrum in table 1.

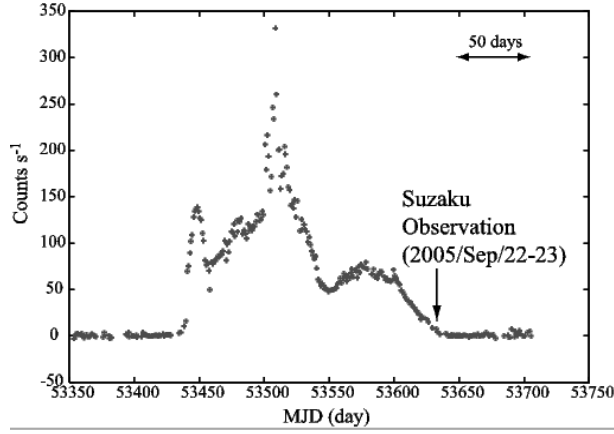


Fig. 1. An X-ray (1.5–12 keV) light curve of GRO J1655–40 obtained by the RXTE ASM. The date of the Suzaku observation is indicated by an arrow.

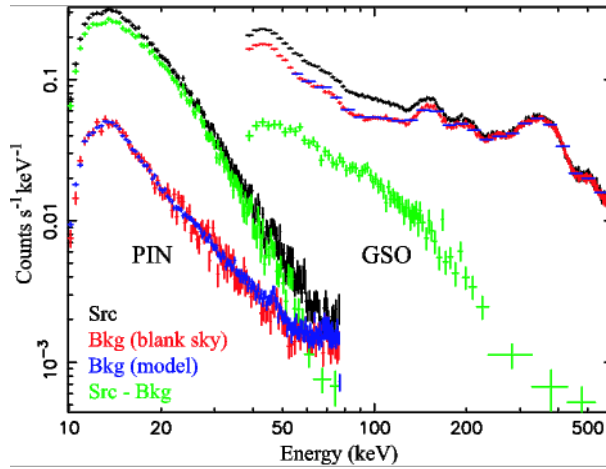


Fig. 2. Background-subtraction procedure for the HXD data. The on-source data, the blank-sky background data, the modeled background data, and the background-subtracted spectra are presented in black, red, blue, and green, respectively. Here and hereafter, the blank-sky data are adopted as the HXD background.

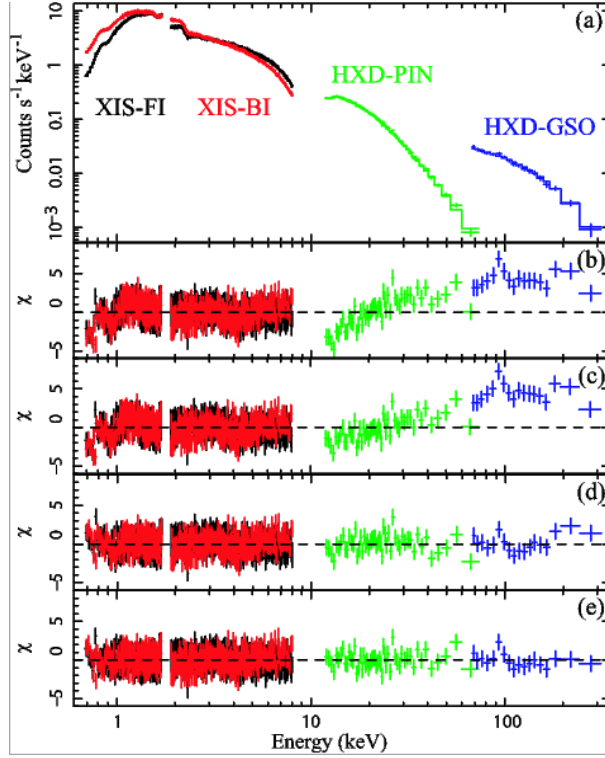


Fig. 3. (a) Background-subtracted broad-band (0.7–300 keV) energy spectra of GRO J1655–40, obtained with the XIS, HXD-PIN (green) and HXD-GSO (blue). The spectra of the FI-CCDs (black) and BI-CCD (red) are plotted separately. The fitting utilized the XIS data in the 0.7–1.7 and 1.9–8 keV ranges, the 12–70 keV PIN data, and the GSO data in the 70–300 keV band. The lower four panels show residuals relative to (b) the “diskbb+compps+gau” model, (c) “diskbb+compps+reflection+gau”, (d) “diskbb+compps+compps+gau”, and (e) “diskbb+compps+compps+reflection+gau”.

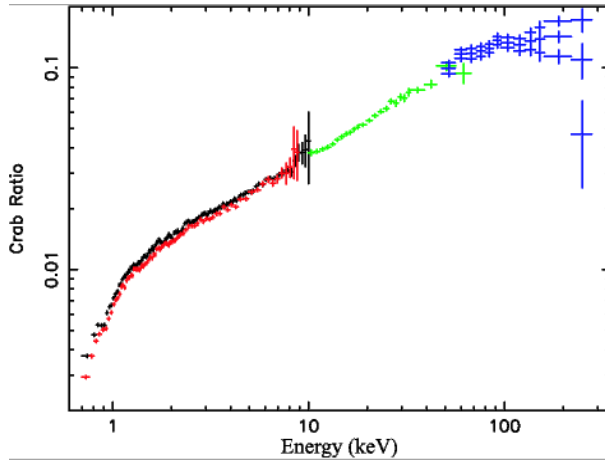


Fig. 4. Time-averaged and background-subtracted spectra of GRO J1655–40, divided by the corresponding spectra of the Crab Nebula. GSO data after artificially changing the normalization of the blank-sky background by $\pm 2\%$ are also shown. The color code is the same as that in figure 3.

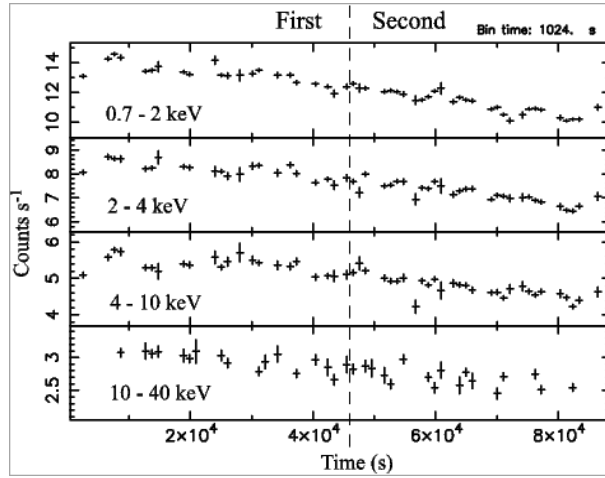


Fig. 5. Background-subtracted light curves of GRO J1655–40 obtained with the XIS1 (0.7–2, 2–4, and 4–10 keV) and PIN (10–40 keV). A vertical line divides the exposure into “first” and “second” halves.

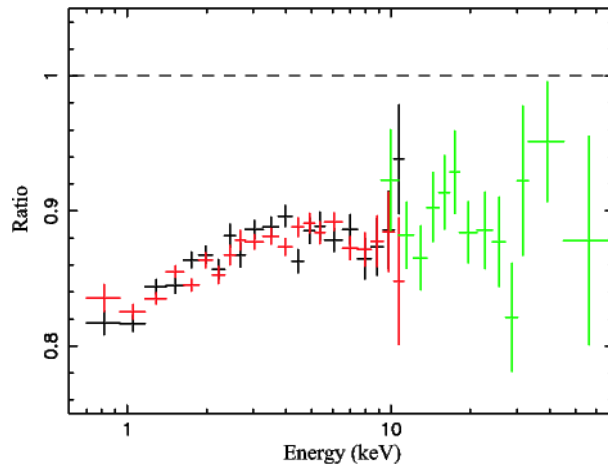


Fig. 6. The background-subtracted spectra of GRO J1655–40 obtained with the XIS and PIN in the second half, divided by those in the first half.

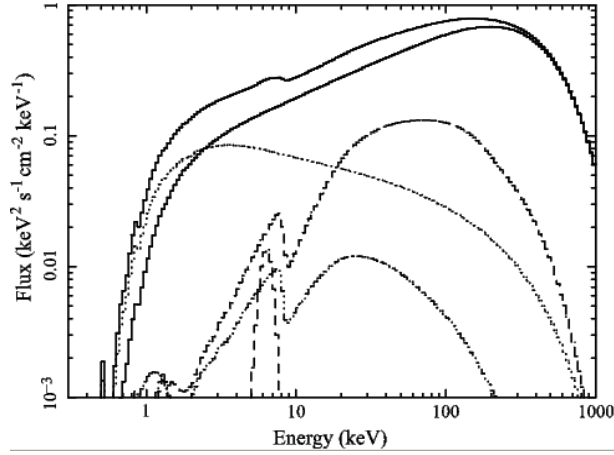


Fig. 7. The “diskbb+compps+compps+reflection+gau” models utilized in figure 3 e. Each spectral component is shown individually.

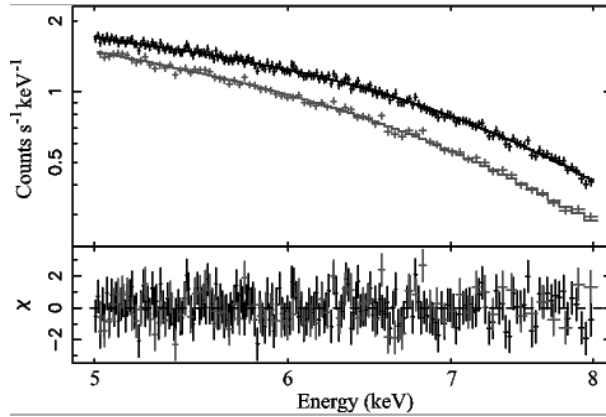


Fig. 8. An expanded presentation of the 5–8 keV portion of the XIS (FI-CCD in black and BI-CCD in grey) spectra. The bottom panel shows the residuals of the data relative to the best-fitting model consisting of a single power-law and a broad Gaussian line.

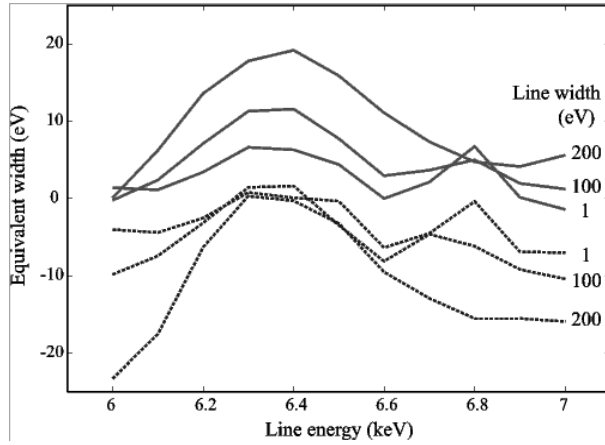


Fig. 9. The 90% confidence upper limits on the equivalent widths of Gaussian emission (solid) or absorption (dotted) lines in the XIS spectra, shown as a function of the assumed line-center energy.

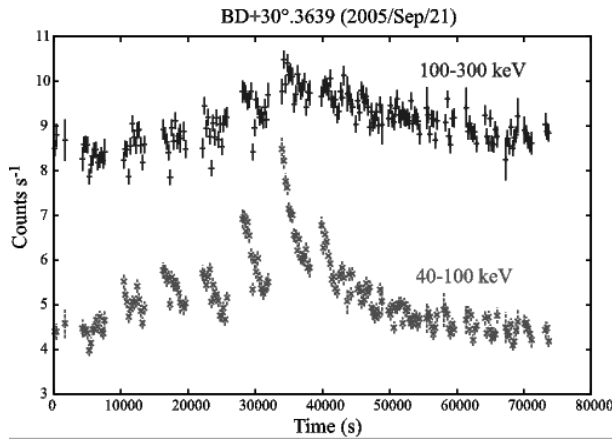


Fig. 10. Blank-sky GSO light curves in the 40–100 keV and 100–300 keV bands, recorded during the observation of BD+30°3639.

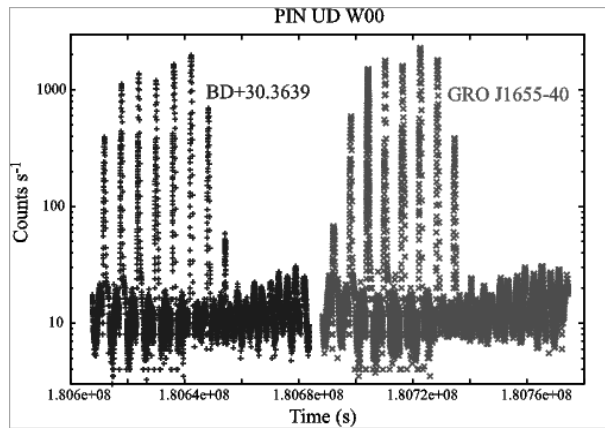


Fig. 11. Light curves of the PIN upper-discriminator counts from the HXD Unit 0, obtained from the observations of GRO J1655–40 (black) and BD+30°3639 (grey).

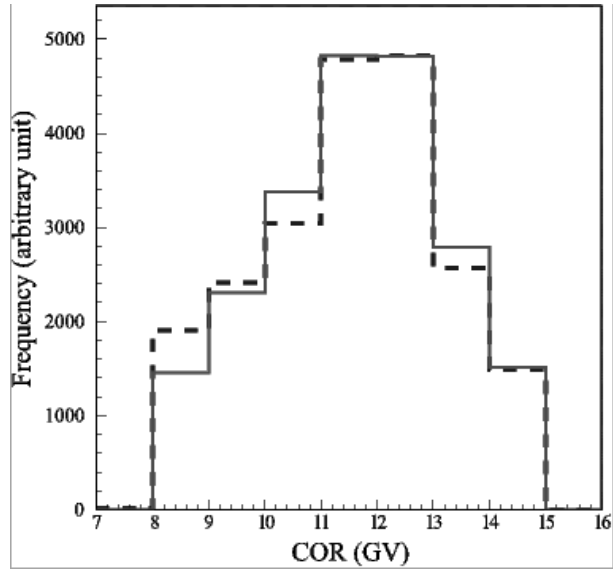


Fig. 12. Distributions of COR during the observations of GRO J1655-40 (solid) and BD+30°3639 (broken). The periods during which the sources were occulted by the Earth were discarded.